Biomedical Optics EXPRESS

Validation of a partial coherence interferometry method for estimating retinal shape

Pavan K. Verkicharla,[1,2] Marwan Suheimat,[1,2] James M. Pope,[2] Farshid Sepehrband,[2,3] Ankit Mathur,[1,2] Katrina L. Schmid,[1,2] and David A. Atchison[1,2,*]

[1]*School of Optometry & Vision Science, Queensland University of Technology, Brisbane, 4059 Australia*
[2]*Institute of Health and Biomedical Innovation, Queensland University of Technology, Brisbane, 4059 Australia*
[3]*Centre for Advanced Imaging, University of Queensland, Brisbane, 4072, Australia*
**d.atchison@qut.edu.au*

Abstract: To validate a simple partial coherence interferometry (PCI) based retinal shape method, estimates of retinal shape were determined in 60 young adults using off-axis PCI, with three stages of modeling using variants of the Le Grand model eye, and magnetic resonance imaging (MRI). Stage 1 and 2 involved a basic model eye without and with surface ray deviation, respectively and Stage 3 used model with individual ocular biometry and ray deviation at surfaces. Considering the theoretical uncertainty of MRI (12-14%), the results of the study indicate good agreement between MRI and all three stages of PCI modeling with <4% and <7% differences in retinal shapes along horizontal and vertical meridians, respectively. Stage 2 and Stage 3 gave slightly different retinal co-ordinates than Stage 1 and we recommend the intermediate Stage 2 as providing a simple and valid method of determining retinal shape from PCI data.

OCIS codes: (330.4460) Ophthalmic optics and devices; (330.7326) Visual optics, modeling.

References and links

1. R. A. Stone and D. I. Flitcroft, "Ocular shape and myopia," Ann. Acad. Med. Singapore **33**(1), 7–15 (2004).
2. W. N. Charman and H. Radhakrishnan, "Peripheral refraction and the development of refractive error: a review," Ophthalmic Physiol. Opt. **30**(4), 321–338 (2010).
3. E. L. Smith 3rd, "Prentice Award Lecture 2010: A case for peripheral optical treatment strategies for myopia," Optom. Vis. Sci. **88**(9), 1029–1044 (2011).
4. J. F. Chen, A. E. Elsner, S. A. Burns, R. M. Hansen, P. L. Lou, K. K. Kwong, and A. B. Fulton, "The effect of eye shape on retinal responses," Clin. Vis. Sci. **7**(6), 521–530 (1992).
5. D. A. Atchison, C. E. Jones, K. L. Schmid, N. Pritchard, J. M. Pope, W. E. Strugnell, and R. A. Riley, "Eye shape in emmetropia and myopia," Invest. Ophthalmol. Vis. Sci. **45**(10), 3380–3386 (2004).
6. D. A. Atchison, N. Pritchard, K. L. Schmid, D. H. Scott, C. E. Jones, and J. M. Pope, "Shape of the retinal surface in emmetropia and myopia," Invest. Ophthalmol. Vis. Sci. **46**(8), 2698–2707 (2005).
7. B. Gilmartin, M. Nagra, and N. S. Logan, "Shape of the posterior vitreous chamber in human emmetropia and myopia," Invest. Ophthalmol. Vis. Sci. **54**(12), 7240–7251 (2013).
8. J. W. Beenakker, D. P. Shamonin, A. G. Webb, G. P. Luyten, and B. C. Stoel, "Automated retinal topographic maps measured with magnetic resonance imaging," Invest. Ophthalmol. Vis. Sci. **56**(2), 1033–1039 (2015).
9. T. Q. Duong, "Magnetic resonance imaging of the retina: A brief historical and future perspective," Saudi J. Ophthalmol. **25**(2), 137–143 (2011).
10. P. K. Verkicharla, A. Mathur, E. A. H. Mallen, J. M. Pope, and D. A. Atchison, "Eye shape and retinal shape, and their relation to peripheral refraction," Ophthalmic Physiol. Opt. **32**(3), 184–199 (2012).
11. M. C. M. Dunne, D. A. Barnes, and R. A. Clement, "A model for retinal shape changes in ametropia," Ophthalmic Physiol. Opt. **7**(2), 159–160 (1987).
12. M. C. M. Dunne, "A computing scheme for determination of retinal contour from peripheral refraction, keratometry and A-scan ultrasonography," Ophthalmic Physiol. Opt. **15**(2), 133–143 (1995).
13. N. S. Logan, B. Gilmartin, C. F. Wildsoet, and M. C. M. Dunne, "Posterior retinal contour in adult human anisomyopia," Invest. Ophthalmol. Vis. Sci. **45**(7), 2152–2162 (2004).
14. G. F. Schmid, "Axial and peripheral eye length measured with optical low coherence reflectometry," J. Biomed. Opt. **8**(4), 655–662 (2003).
15. G. F. Schmid, "Variability of retinal steepness at the posterior pole in children 7-15 years of age," Curr. Eye Res. **27**(1), 61–68 (2003).

#241860 Received 27 May 2015; revised 28 Jul 2015; accepted 30 Jul 2015; published 5 Aug 2015

16. G. F. Schmid, "Association between retinal steepness and central myopic shift in children," Optom. Vis. Sci. **88**(6), 684–690 (2011).
17. E. A. H. Mallen and P. Kashyap, "Technical note: Measurement of retinal contour and supine axial length using the Zeiss IOLMaster," Ophthalmic Physiol. Opt. **27**(4), 404–411 (2007).
18. D. A. Atchison and W. N. Charman, "Can partial coherence interferometry be used to determine retinal shape?" Optom. Vis. Sci. **88**(5), E601–E607 (2011).
19. A. Ehsaei, C. M. Chisholm, I. E. Pacey, and E. A. H. Mallen, "Off-axis partial coherence interferometry in myopes and emmetropes," Ophthalmic Physiol. Opt. **33**(1), 26–34 (2013).
20. M. Faria-Ribeiro, A. Queirós, D. Lopes-Ferreira, J. Jorge, and J. M. González-Méijome, "Peripheral refraction and retinal contour in stable and progressive myopia," Optom. Vis. Sci. **90**(1), 9–15 (2013).
21. X. Ding, D. Wang, Q. Huang, J. Zhang, J. Chang, and M. He, "Distribution and heritability of peripheral eye length in Chinese children and adolescents: the Guangzhou Twin Eye Study," Invest. Ophthalmol. Vis. Sci. **54**(2), 1048–1053 (2013).
22. L. A. Cameron, L. S. Gray, D. Seidel, and M. Day, "The effect of measurement assumptions when investigating peripheral eye length and peripheral refraction," (*Ophthalmic Physiol Opt*, Glasgow, 2013), p. 112.
23. P. K. Verkicharla, E. A. H. Mallen, and D. A. Atchison, "Repeatability and comparison of peripheral eye lengths with two instruments," Optom. Vis. Sci. **90**(3), 215–222 (2013).
24. P. K. Verkicharla, M. Suheimat, E. A. Mallen, and D. A. Atchison, "Influence of eye rotation on peripheral eye length measurement obtained with a partial coherence interferometry instrument," Ophthalmic Physiol. Opt. **34**(1), 82–88 (2014).
25. S. Kasthurirangan, E. L. Markwell, D. A. Atchison, and J. M. Pope, "In vivo study of changes in refractive index distribution in the human crystalline lens with age and accommodation," Invest. Ophthalmol. Vis. Sci. **49**(6), 2531–2540 (2008).
26. D. A. Atchison and G. Smith, *Optics of the Human Eye* (Butterworth-Heinemann, Oxford, 2000).
27. M. Suheimat, P. K. Verkicharla, E. A. Mallen, J. J. Rozema, and D. A. Atchison, "Refractive indices used by the Haag-Streit Lenstar to calculate axial biometric dimensions," Ophthalmic Physiol. Opt. **35**(1), 90–96 (2015).
28. D. A. Atchison and G. Smith, "Chromatic dispersions of the ocular media of human eyes," J. Opt. Soc. Am. A **22**(1), 29–37 (2005).
29. X. Adnan, M. Suheimat, N. Efron, K. Edwards, N. Pritchard, A. Mathur, E. A. Mallen, and D. A. Atchison, "Biometry of eyes in type 1 diabetes," Biomed. Opt. Express **6**(3), 702–715 (2015).
30. A. N. Kuo, R. P. McNabb, S. J. Chiu, M. A. El-Dairi, S. Farsiu, C. A. Toth, and J. A. Izatt, "Correction of ocular shape in retinal optical coherence tomography and effect on current clinical measures," Am. J. Ophthalmol. **156**(2), 304–311 (2013).
31. A. Podoleanu, I. Charalambous, L. Plesea, A. Dogariu, and R. Rosen, "Correction of distortions in optical coherence tomography imaging of the eye," Phys. Med. Biol. **49**(7), 1277–1294 (2004).
32. R. J. Zawadzki, A. R. Fuller, S. S. Choi, D. F. Wiley, B. Hamann, and J. S. Werner, "Correction of motion artifacts and scanning beam distortions in 3D ophthalmic optical coherence tomography imaging," in Biomedical Optics (BiOS) 2007 (International Society for Optics and Photonics, 2007), pp. 642607–642607–642611.

1. Introduction

The mechanisms for development of myopia remain unclear. Most attention has been given to the fovea and focus state along the visual axis, but as the foveal area forms only a small part of the visual field it is reasonable that the peripheral retina and its imaging might contribute to refraction determination. Recent research has pointed to retinal shape being an important consideration in myopia development [1–3].

There have been a few studies of retinal shape using magnetic resonance imaging [4–8]. The technique suffers from high cost of up to AUD $500/scan, long testing time of 2-3 minutes per image, and low resolution of approximately 0.15 mm [9]. A simpler method that is inexpensive and accurate will be of considerable value to myopia research.

Retinal or overall eye shape has been inferred from peripheral refraction relative to central refraction; for example, negative relative peripheral refraction is associated with a "prolate" shape [10]. Given that the eye's optics, as well as the retinal shape, contributes to the peripheral refraction, this inference should be made cautiously. Dunne [11, 12] developed a sophisticated method in which a model eye was customized with anterior corneal curvature and intraocular distances matching individual data, and the anterior corneal asphericity and retinal shape were manipulated during raytracing until model peripheral refractions matched those of experimental data. This method was used in subsequent studies [11–13].

Retinal shape has also been estimated from partial coherence interferometry [14–21] using commercial instruments such as the IOLMaster (Carl-Zeiss Meditec AG Jena, Germany) and

#241860 Received 27 May 2015; revised 28 Jul 2015; accepted 30 Jul 2015; published 5 Aug 2015

the Lenstar LS900 biometer (Haag Streit, Bern, Switzerland). These instruments provide better resolution (0.01-0.02 mm) for both central and peripheral eye lengths than magnetic resonance imaging. Theoretical investigations of the PCI technique indicated that it can give accurate results for retinal shape [18, 22], but there are some assumptions in its use such as the refractive index, used to convert from optical path lengths to distances, and deviation of light beams inside the eye.

Neither peripheral refraction nor partial coherence interferometry based techniques for determining retinal shape have been assessed for validity against magnetic resonance imaging. The purpose of this study is to develop and evaluate a simple method of determining retinal shape using partial coherence interferometry. Dunne's method using peripheral refraction [12] was also compared with magnetic resonance imaging.

2. Methods

2.1 Participants

Sixty participants including 30 emmetropes (spherical equivalent refraction + 0.75 D to −0.62 D) and 30 myopes (–1.25 D to −8.25 D) were recruited for this study. Mean age of participants was 22.5 ± 3.1 years (range 18 to 28 years). The study followed the tenets of the declaration of Helsinki and the experimental protocols were approved by the Human Research Ethics Committee of the Queensland University of Technology and the University of Queensland. The nature of experimental procedures was explained to participants and written informed consent was obtained before taking measurements.

2.2 Peripheral eye length and peripheral refraction

Peripheral eye lengths and peripheral refractions along the horizontal and vertical meridians of the visual field out to ± 35° and ± 30°, respectively in 5° steps, were obtained for each participant after pupil dilation by a drop of 1.0% tropicamide. The methodology for peripheral eye lengths using the Lenstar biometer and partial coherence interferometry (PCI) has been described fully elsewhere [23, 24]. Peripheral refraction was determined with an SRW-5000 open field auto-refractor (Shin Nippon, Japan). Along the horizontal meridian, participants rotated their eyes to fixate targets on a wall 3 meters away. Along the vertical meridian, targets were placed on a vertical wall 1.67 meters to the side of participants and were viewed through a 45° inclined beam-splitter between the eye and instrument.

2.3 Magnetic resonance imaging (MRI) protocol

MRI was undertaken at the University of Queensland Centre for Advanced Imaging with a Siemens Trio 3.0 Tesla (Siemens, Ehrlangen, Germany), whole-body clinical magnetic resonance imaging system using a standard Siemens 4.0 cm receive only radiofrequency surface coil positioned over the eye by following a procedure that was used previously [5, 6, 25]. Scanning was performed with participants lying supine and looking at a Maltese cross target projected onto a translucent screen at a viewing distance of 0.93 meters. Participants looked upwards to view the target through an adjustable mirror mounted at 45° to the vertical. The surface coil was taped over the participant's right eye. Heads were immobilized with appropriate padding and non-tested eyes were occluded with an eye patch. Participants were asked to fixate the target and minimize blinking during data acquisition. Between acquisitions they were advised to close their eyes and blink freely in order to renew the tear film. For myopes requiring correction < −1.0 D, trial lenses on top of the coil provided a clear target. The distance between the eye and correcting lenses was estimated to be approximately 25 mm, and this was used as a basis for determining lens power (to account for vertex distance).

The standard imaging protocol started with fast localizer scans obtained in three orthogonal planes in few seconds to locate the position of the eye in the center of the field of view. A T2-weighted half-Fourier acquisition single shot turbo spin echo (HASTE) sequence

#241860 Received 27 May 2015; revised 28 Jul 2015; accepted 30 Jul 2015; published 5 Aug 2015

was used to generate 3D isotropic images of the eye with 0.5 mm cubic voxels (128 × 128 × 64 matrix; TR = 2500 ms; TE = 56 ms; imaging time 4 min).

2.4 Retinal shape estimation

From peripheral eye length measurements, estimates of vertex radius of curvature (r_{xv} and r_{yv}) and asphericity (Q_x and Q_y) along the horizontal (x) and vertical (y) meridians were determined in three stages, or approaches, of different sophistication using variations of the four-refracting surface Le Grand *full theoretical eye* [26]. Using the assumption that the Lenstar beams strike the anterior cornea normally, rays were directed towards the point on the axis corresponding to the sagittal center of curvature of this surface and then into the eye to estimate retinal co-ordinates. Using a Solver template in Excel, these were fitted to a conic equation

$$z = \frac{C_v (y - y_0)^2}{1 + \sqrt{1 - (1+Q) C_v^2 (y - y_0)^2}} - \frac{C_v y_0^2}{1 + \sqrt{1 - (1+Q) C_v^2 y_0^2}} \quad (1)$$

where z is surface sag co-ordinate, C_v is vertex curvature, Q is asphericity, y is co-ordinate along the Y-axis (or X-axis) and y_0 is an offset so the retinal center has co-ordinates (0, 0).

For PCI analysis, equations to determine retinal co-ordinates relative to the fovea for a ray subtending an angle θ to the axis were based on those published by Atchison and Charman [18]. Relevant parameters for the three stages are given in the following text and Fig. 1.

The PCI *Stage 1* analysis used only the anterior corneal surface of the eye (spherical, radius of curvature 7.8 mm) and had no light deviation within the eye. Simplification of the Atchison and Charman equations is possible for a spherical cornea (corneal asphericity Q_c = 0). As the Lenstar gives eye length measurements, ignoring the refractive indices of the ocular media and conversion to optical path lengths, Eqs. (1) to (12) of the paper can be replaced by

$$y_r = (AL'_p - r_{cv}) \sin\theta \quad (2)$$

$$\Delta z_3 = r_{cv}(1 - \cos\theta) + AL'_p \cos\theta - AL'_a \quad (3)$$

where AL'_a and AL'_p are on-axis and off-axis eye length measurements, respectively, r_{cv} is the corneal anterior vertex radius of curvature of the model, and co-ordinates (y_r, Δz_3) are equivalent to (y, z) in Eq. (1).

The PCI *Stage 2* analysis used complete model eye parameters and deviation of the light beam was allowed to occur at surfaces except at the anterior cornea. Raytracing was performed using the optical design program Zemax (version 10.0, 2011). As the refractive indices of the ocular media used by the Lenstar are not physiological [27], the refractive indices of the model eye at 555 nm were converted to 820 nm using the Cauchy equation and Table 5 of Atchison and Smith [28] with appropriate scaling where the refractive index of the model at 555 nm was not the same as the reference index in the table. This gave indices at 820 nm of n_{corn} 1.3707, n_{aq} 1.3312, n_{lens} 1.4134, and n_{vitr} 1.3298. For each object angle, raytracing was done through the center of a stop placed at the center of curvature of the cornea, with variation in position of a flat retina until retinal co-ordinates corresponded to measured peripheral eye lengths.

For object angle θ and for a Le Grand model eye with axial length AL_a and a flat retina, in Zemax, peripheral length AL_p, image angle ϕ and retinal co-ordinates (y, 0) were determined by ray-tracing. For an eye with measured peripheral length AL'_p, retinal co-ordinates (y_r, z_r) were

$$(y_r, z_r) = (y + (AL'_p - AL_p)\sin\phi, 0 + (AL'_p - AL_p)\cos\phi) \quad (4)$$

#241860 Received 27 May 2015; revised 28 Jul 2015; accepted 30 Jul 2015; published 5 Aug 2015

For a real eye with the central axial length of AL'_a rather than AL_a, the retinal co-ordinates changed to new retinal co-ordinates (y_r', z_r'), where

$$(y_r', z_r') = (y_r, z_r - (AL'_a - AL_a)) = (y + (AL'_p - AL_p)\sin\phi, (AL'_p - AL_p)\cos\phi - (AL'_a - AL_a)) \quad (5)$$

For the PCI *Stage 3* analysis, many Le Grand full schematic eye components were replaced with individual eye data: the anterior corneal topography (average of four topography results obtained from Medmont E300 corneal topographer), the posterior cornea radius of curvature (from Pentacam topography, spherical surface used by averaging across the meridians), anterior and posterior lens radii of curvatures (phakometry), equivalent lens refractive index (phakometry), and intra-ocular axial distances within the eye (Lenstar). The phakometry technique with its determination of anterior and posterior lens radii of curvatures and lens equivalent index has been described elsewhere [29].

It was assumed that the on-axis measurement with the Lenstar corresponded to the corneal topographic axis and thus corneal topography data were neither tilted nor decentered. A custom built MATLAB (Mathworks, Natick, MA) program in combination with Zemax was used to produce a variable corneal "sagittal center of curvature" as the stop and first surface to ensure no deviation at the anterior cornea. This used calculation of the surface slopes at various positions on the surface. The on-axis vitreous length was estimated as

$$v_a = AL'_a - (CCT_a + ACD_a + LT_a)$$

where AL'_a is again the on-axis length measurement as in Stage 2 and CCT_a, ACD_a and LT_a are on-axis distances within the cornea, anterior chamber and lens. The peripheral vitreous length was estimated as

$$v_p = AL'_p - (CCT_p + ACD_p + LT_p)$$

where AL'_p is again the off-axis eye length measurement as in Stage 2 and CCT_p, ACD_p and LT_p are peripheral distances within the cornea, anterior chamber and lens. Using the image space angle ϕ, the off-axis retinal co-ordinates (y_r', z_r') are given by

$$z_r' = v_p\cos\phi + z_4 - v_a \quad (6)$$

$$y_r' = y_4 + v_p\sin\phi \quad (7)$$

where (z_4, y_4) are chief ray co-ordinates at the posterior lens surface (relative to its vertex).

2.5 Dunne's method

Dunne's method [11, 12] modifies the Gullstrand-Emsley three refracting-surface model eye [26] according to measured anterior corneal radius of curvature and internal ocular distances. Out-of-the-eye ray-tracing was done at each visual field angle for the meridian of interest. Corneal asphericity for each visual field angle was manipulated until peripheral astigmatism matched its measurement for a retina with a (–)12 mm radius of curvature. Retinal radius of curvature for each angle, and consequently retinal co-ordinate intersection with the chief ray, were altered until the sagittal refraction matched its measurement (refraction at right angles to the visual field meridian). The curvatures of the lens surfaces were selected so that the ratio of the surface curvatures matched those of the lens in the Gullstrand-Emsley model eye. Equation (1) was applied to the set of retinal co-ordinates to obtain conic fits.

2.6 MRI image analysis

MRI data were analyzed using custom written MATLAB® (Mathworks, Natick, MA) software. The major steps were: image referencing to estimated foveal position, retina

#241860 Received 27 May 2015; revised 28 Jul 2015; accepted 30 Jul 2015; published 5 Aug 2015

segmentation to extract retina boundaries, and data fitting to estimate the vertex radius of curvature and asphericity.

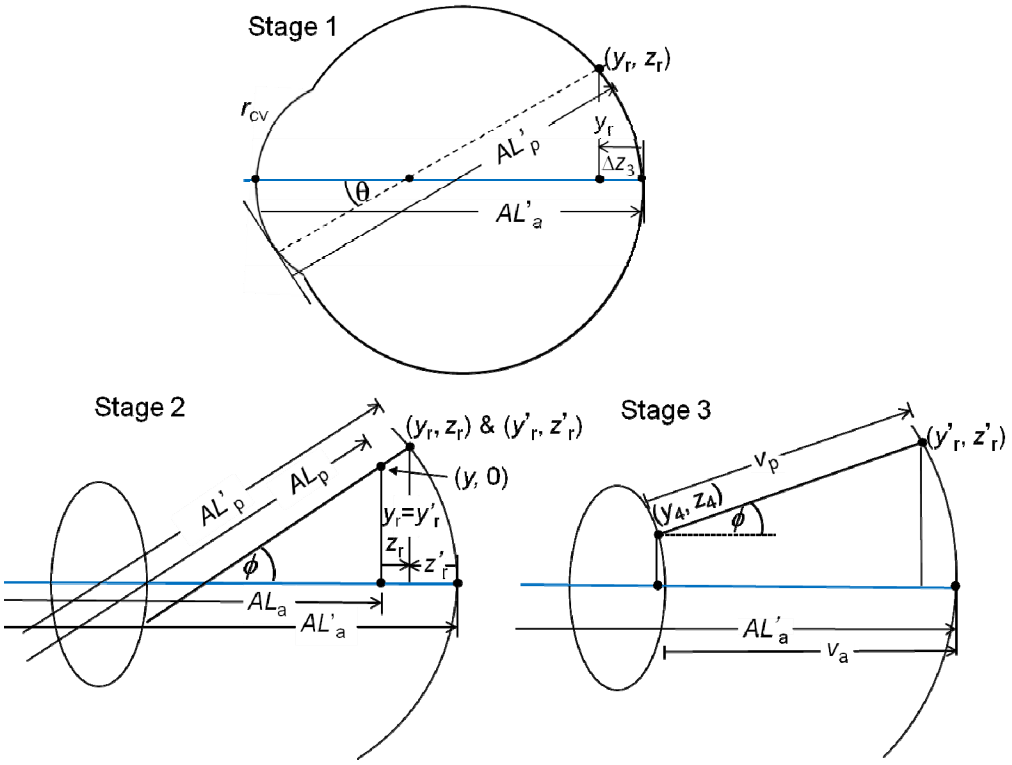

Fig. 1. Parameters used for determination of retinal co-ordinates in Stage 1, Stage 2 and Stage 3 modeling. Details are given in the text.

The 3D images obtained from MRI had limited resolution (0.5 mm) and it was not possible to identify the fovea directly. Foveal position was estimated based on the position of optic nerve that was seen in all MRI images (optic nerve is approximately 15° nasal to the fovea relative to the posterior pole of the lens). All images were rotated so that the retinal shape estimates were determined with reference to the visual axis through the fovea, rather than to the "optical axis" that was the best estimate of the axis passing through the cornea and lens and cornea. The two axes were a mean 3.5° apart.

The retinal boundary was segmented in each slice by applying a Canny edge detection algorithm to determine the transition between voxels that are solely in the vitreous to those that are solely in the sclera. In order to decrease the influence of partial volume effects, the retina was segmented in all three planes (axial, sagittal and coronal). All the acquired boundary points were concatenated to build an N × 3 matrix in the co-ordinate system, where N denotes the number of segmented voxels. The dimensions of the (cubic) voxels in the 3D HASTE images were 0.5 mm. Since the retina and choroid are ~0.2 mm thick, edge voxels typically extend from the vitreous, through the retina and choroid and into the sclera. The edges found were therefore most likely to be approximately mid-way between the vitreous/retinal boundary and the choroid/sclera boundary. To find the centre slice accurately, we fitted the retina boundary points to a simple symmetric 3D ellipse.

The vertex radius of curvature and asphericity were determined for 11 different fractions F of the eye ranging from F = 25% to F = 75% in 5% steps calculated by fitting the segmented boundary points of the retina. The fraction was defined with reference to the center point 'o' of the eye on the visual axis (Fig. 2). The desired fraction was extracted by masking out the

#241860 Received 27 May 2015; revised 28 Jul 2015; accepted 30 Jul 2015; published 5 Aug 2015

remaining portion of the eye. For a spherical eye, the general relationship between the *fractional area F* and the angle subtended at the center of the eye (θ_1) is given by:

$$F = 100\% \times [1 - \cos(\theta_1 / 2)] / 2 \quad (8)$$

This relationship was used to calculate the angles θ_1 corresponding to a given fraction of the retina. For example, the angles associated with F = 25%, 35% and 75% are θ_1 = 120°, 145° and 240°, respectively (Fig. 2). Due to the need to exclude the corneal 'bulge', the largest fraction that could consistently be employed in fitting the eye shapes was F = 75%.

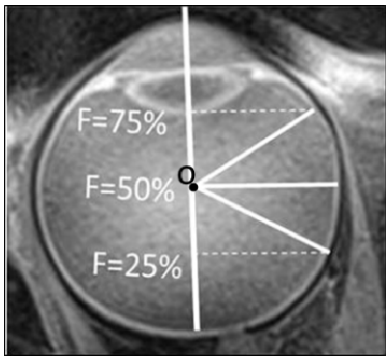

Fig. 2. Fractions of eye (F) used to determine retinal shape estimates with MRI, the maximum being 75% and the minimum being 25%.

All the selected voxels were arranged into an N × 3 matrix, representing the retinal points and the non-linear least squares fitting of the data were made to the equation

$$C_x^2 X^2 + C_y^2 Y^2 + C_z^2 Z^2 - 2C_z Z = 0 \quad (9)$$

where $C_x = 1/R_x$, $C_y = 1/R_y$ and $C_z = 1/R_z$. Using these parameters, vertex radii of curvature in the XZ and YZ planes were $r_{xv} = R_x^2/R_z$ and $r_{yv} = R_y^2/R_z$, respectively, with corresponding asphericities $Q_x = R^2_x/R^2_z - 1$ and $Q_y = R^2_y/R^2_z - 1$. The coefficient of determination (R^2), the square of the correlation between the retinal co-ordinates and their fitted values, was used to evaluate the goodness of fit.

For the best comparison between MRI- and PCI-derived retinal shapes, similar regions should be used. PCI eye length measurements were obtained to ± 35° (central 70°), where this angle is referenced to the center of curvature of the cornea, which is conveniently close to the posterior nodal point and posterior lens vertex. With reference to Fig. 3, the tangents of the angles θ_1 and θ_2 subtended at the center of the eye and posterior nodal point, respectively, to give the same retinal region are related to the corresponding distances by

$$\theta_1 = 2\tan^{-1}[\tan(\theta_2 / 2) l_2 / l_1] \quad (10)$$

Here distance l_1 is the vertex radius determined using axially symmetrical fits with MRI data. The distance l_2 for the PCI data is approximately related to the axial length AL'_a by

$$l_2 = AL'_a - 7.8 \quad (11)$$

The distance 7.8 mm in the equation corresponds to the center of curvature of the cornea, which is conveniently close to the posterior nodal point and posterior lens vertex.

For 60 participants, θ_1 was estimated to range from 116° to 136° (mean ± 95% CI = 124° ± 1°) for θ_2 = 70° (horizontal meridian). From Eq. (8), this corresponds to a fraction F = 27%. Based on a simple proportions, the fraction for the vertical meridian (θ_2 = 60°) is approximately 23%. This is close to the minimum fraction of the eye that was analyzed with MRI (25%). However MRI data corresponding to less than 35% resulted in very poor R^2

#241860 Received 27 May 2015; revised 28 Jul 2015; accepted 30 Jul 2015; published 5 Aug 2015

values in a few cases and therefore, the MRI data for F = 35% were used for the comparison with PCI. The retinal region for Dunne's method matched that for PCI approximately.

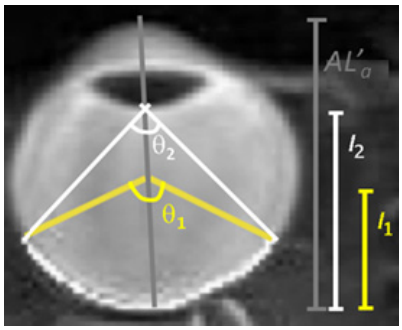

Fig. 3. Angles and distances used to define similar retinal regions for comparison between PCI and MRI. θ_1 and θ_2 are the angles subtended approximately at the center of the eye (MRI) and at the posterior lens vertex (PCI), l_1 and l_2 are the corresponding distances, and AL'_a is the axial length of the eye obtained from the Lenstar.

2.7 Comparison of methods

The different methods for determining the retinal surface were compared using the vertex radius of curvature (r_v) and asphericity (Q) derived from fitting. However, r_v and Q are not independent of each other; for example, a positive change in Q can compensate for a positive change in r_v. A tool to consider r_v and Q together was desirable. For this reason, the estimated parameters along each meridian were combined to form a "surface shape" and agreements between MRI and PCI estimates and between MRI and Dunne's method were given as "percentage differences" between surface shapes using Eq. (12). Substituting values for C_v ($1/r_v$) and Q in Eq. (1), retinal surface shapes for each participant along both meridians obtained from PCI and MRI methods were re-constructed in MATLAB. The comparison was made by taking the average of point-by-point height differences between the two surfaces over a distance of 15.6 mm (7.8 mm either side of the peak) and giving this as a percentage of the sagittal heights across the distance:

$$\text{Percentage difference} = \frac{\frac{\sum_{i=1}^{n}\left|z_{i,PCI} - z_{i,MRI}\right|}{N}}{0.5\times\left(sag_{PCI} + sag_{MRI}\right)}\times 100\% \qquad (12)$$

where $Z_{i,PCI}$ and $Z_{i,MRI}$ are z-co-ordinates for the i th point using the PCI MRI fits, sag_{PCI} and sag_{MRI} are the sagittal heights of the PCI and MRI fits, and N is the number of sampled points (1561). Fig. 4 shows two curves representing retinal surface shapes estimated from the MRI and one of the PCI stages for one participant.

The "percentage difference" approach does not indicate if one surface shape is consistently flatter than another. Therefore, another parameter called "ratio of areas under the surface shapes" was determined in which the areas under the surface shapes obtained by PCI, MRI and Dunne's method were compared. To determine the areas, the region under the surface shape was divided into multiple narrow rectangles, of width 0.01 mm, whose areas were added. The two surface shapes started from the same vertex and the areas under the two surface shapes were calculated with reference to the surface shape that had the greatest sag. For example, in Fig. 4 the reference is the MRI derived surface and the area under the flatter PCI surface shape is greater than the area under the MRI surface shape. The ratio of areas under the surface shapes for each PCI Stage and for Dunne's method were determined as PCI/MRI and Dunne's Method/MRI along the horizontal and vertical meridians.

#241860 Received 27 May 2015; revised 28 Jul 2015; accepted 30 Jul 2015; published 5 Aug 2015

Comparisons of retinal shape estimates between PCI and MRI, and between Dunne's method and MRI, were determined using paired *t*-tests for r_v and Q. The agreement between the methods was also assessed by the "percentage difference" and "ratio of areas under the surface shapes" approaches.

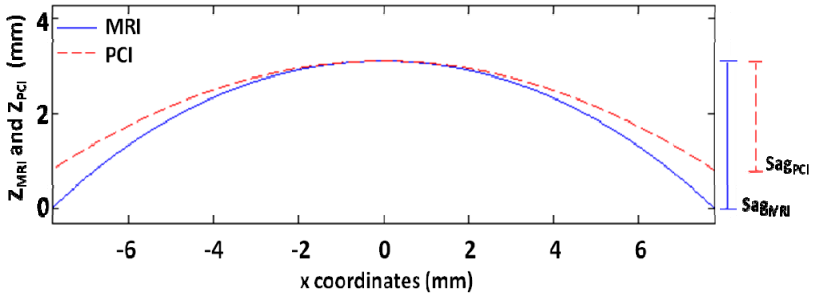

Fig. 4. Retinal surface shapes from MRI and one of the PCI stages for one participant. The blue solid line and the red dotted line represent the MRI and PCI estimates, respectively.

3. Results

Two participants whose retina shapes were estimated using MRI had R^2 values < 0.6 (poor quality images due to motion artefacts) and were not included when comparing PCI and MRI estimates. R^2 values for the other 58 participants were > 0.7 (mean 0.92) at F = 35%.

3.1 PCI estimates

Figure 5 shows means ± SD of the retinal co-ordinates derived from the three stages of modeling from 58 participants along the horizontal and vertical meridians. The Z retinal co-ordinates became more negative and the X/Y co-ordinates shifted laterally with increasing level of sophistication from Stage 1 to 2, but there was little change in mean retinal steepness. The differences between Stages 2 and 3 estimates were slight.

The "ratios of the areas under the surface shapes" approach was used to investigate relative steepness of the surfaces determined by the different stages. Mean ± 95% confidence limits of ratios of areas under surface shape for Stage 1 and Stage 2 (Stage 1/Stage 2) along the horizontal and vertical meridians were 1.00 ± 0.01 and 1.00 ± 0.01, respectively; the corresponding ratios for Stage 2 and Stage 3 (Stage 2/Stage 3) were 1.02 ± 0.01 and 1.00 ± 0.02, which means that the Stage 2 provides significantly, although slightly, flatter shapes than Stage 3 along the horizontal meridian.

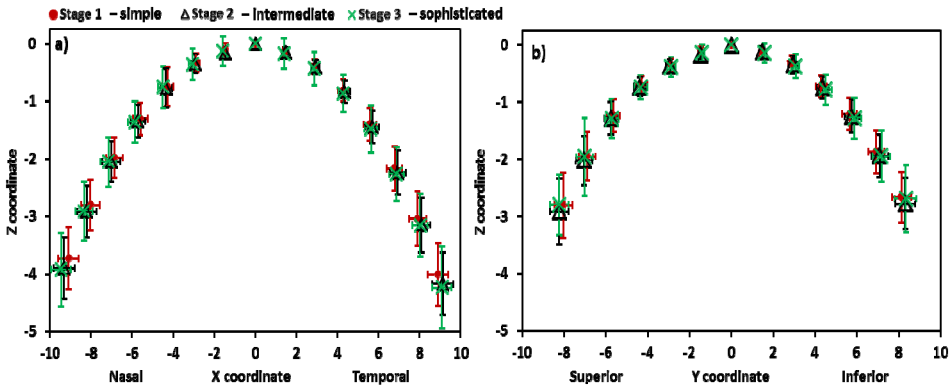

Fig. 5. Retinal co-ordinates in the three stages of PCI modeling along a) the horizontal meridian, and b) the vertical meridian. Horizontal and vertical error bars represent standard deviations for Z and X/Y co-ordinates, respectively.

#241860 Received 27 May 2015; revised 28 Jul 2015; accepted 30 Jul 2015; published 5 Aug 2015

3.2 MRI versus PCI estimates

Differences of retinal shape estimates r_v and Q between MRI and PCI were similar for all three stages of PCI modeling (Table 1). Differences were smaller along the horizontal meridian than along the vertical meridian. Paired t tests showed statistically significant differences for r_{xv}, Q_x and Q_y between MRI and Stage 3, but not between MRI and either Stage 1 or Stage 2. r_{yv} was significantly different between MRI and all three stages of PCI modeling.

Table 1. Differences (mean ± 95% confidence limits) of retinal shape estimates between MRI and the three stages of PCI modeling. * p < 0.05.

Estimate	MRI - $PCI_{Stage\ 1}$	MRI - $PCI_{Stage\ 2}$	MRI - $PCI_{Stage\ 3}$
r_{xv} (mm)	–0.2 ± 0.5	–0.4 ± 0.5	+ 0.8 ± 0.5*
Q_x	–0.04 ± 0.21	–0.00 ± 0.21	+ 0.74 ± 0.15*
r_{yv} (mm)	–1.7 ± 0.5*	–1.7 ± 0.5*	–1.6 ± 0.7*
Q_y	–0.11 ± 0.32	–0.07 ± 0.29	+ 0.43 ± 0.27*

Differences of retinal shape estimates between MRI and the three stages of PCI modeling, using the "percentage difference" approach, are shown in Fig. 6. Mean ± 95% confidence limits of the differences along the horizontal meridian were 3.8 ± 0.7%, 3.7 ± 0.6% and 3.5 ± 0.6% for Stages 1, 2, and 3, respectively; corresponding values for the vertical meridian were 5.6 ± 0.9%, 6.2 ± 1.1% and 6.2 ± 1.0%.

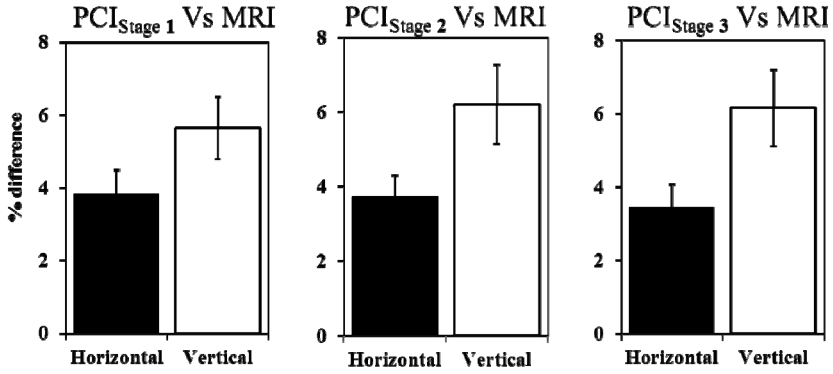

Fig. 6. Mean difference in retinal surface estimates, using the "percentage difference" approach, between MRI and PCI Stages 1, 2 and 3. Error bars are 95% confidence intervals of means.

Using the "ratio of the areas under the surface shapes" approach, all three stages of PCI modeling generally had larger areas (flatter shapes) than MRI with this being more pronounced along the vertical than along the horizontal meridian. Mean ± 95% CI of ratio of areas between Stages 1, 2, 3, in order, and MRI along the horizontal meridian were 1.01 ± 0.02, 1.01 ± 0.02, and 0.99 ± 0.02, respectively; corresponding ratios for vertical meridian were 1.05 ± 0.02, 1.06 ± 0.02, and 1.06 ± 0.02.

3.3 MRI versus Dunne's method

Mean difference ± 95% CI for r_v and Q along the horizontal meridian were –1.7 ± 0.6 mm and –0.15 ± 0.29, respectively; corresponding values along the vertical meridian were –3.1 ± 0.7 mm and –0.60 ± 0.45. The two methods gave significantly different results for all parameters except for asphericity Q_x along the vertical meridian (p = 0.15). Mean ± 95% CI differences of retinal shape estimates between MRI and Dunne's method, using the "percentage difference" approach, were 6.0 ± 1.2% horizontally and 8.9 ± 1.1% vertically,

#241860 Received 27 May 2015; revised 28 Jul 2015; accepted 30 Jul 2015; published 5 Aug 2015

which are about 1.5 times the differences between MRI and any of the PCI stages. Using the "Ratios of the areas under the surface shapes" approach, Dunne's method had larger areas (flatter shapes), with the mean ± 95% CI of the ratio of areas being 1.07 ± 0.01 horizontally and 1.09 ± 0.02 vertically, which are greater than the ratio of areas between MRI and any of the PCI stages.

3.4 Uncertainty with MRI

Uncertainty of retinal shape estimates with MRI was determined by taking into consideration that dimensions of the cubic voxels in 3D HASTE images were 0.5 mm. A simple model with a spherical retinal surface having a radius of curvature of 12 mm over a distance of 15.6 mm (7.8 mm either side from center) was used to determine surface co-ordinates using Eq. (1). The 7.8 mm distance, smaller than the smallest radius of curvature in the data set of 58 participants (8.5 mm), was chosen to maintain a 1:1 relationship between Y and Z co-ordinates.

Figure 7 shows three fits where the blue curve assumes the points at the center of MRI voxels for both the center and edge of the curve, the green curve assumes the upper edge of the voxel at the center of the curve and the lower edge of the voxel at the edges of the curve, and the red curve assumes the opposite to the green curve. The green and red curves were repositioned to have the same vertex as the one passing through the center of the voxel (blue curve). Pushing the central point up by 0.25 mm and the edges down by the same amount (green curve) and smoothing the curve between them after repositioning produced r_v = 8.36 mm, Q = –1.51 with Eq. (1). Pushing the central point down and the edges up (red curve) produced r_v = 17.18 mm with Q = + 2.96. Comparing these values using Eq. (12) gives the percentage difference (uncertainty) between green and red curves of 14.1%. Fitting the co-ordinates to a best circle (Q = 0) gave equivalent radii of curvature of 10.27 (green curve) and 14.67 (red curve) with uncertainty of 12%.

The estimates above assume the voxel counts as edge voxels that form the retinal boundary (for the edge/boundary detection algorithm, edge voxels are between vitreous and sclera) irrespective of the amount of the voxel enclosed inside it. As the edge detection algorithm has a thresholding condition, this assumption gives the maximum possible differences that could occur in retinal shape due to the partial volume effect on MRI. Therefore, the percentages above are exaggerations of the uncertainty in the most extreme cases (from 0% - 100% of the voxels filled).

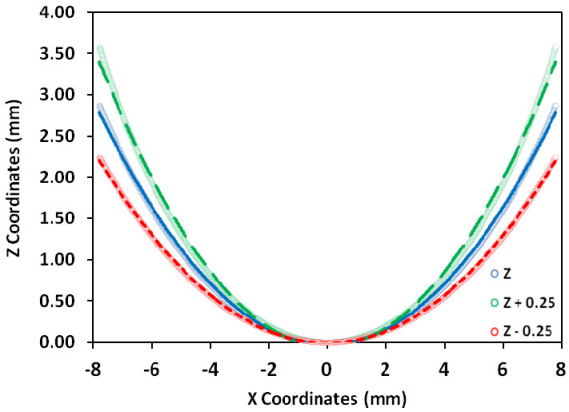

Fig. 7. Retinal surface co-ordinates corresponding to center of voxels for both the center and edge of the curve (blue) and at the opposite extremes of the 0.5 mm voxels (green curve: Z + 0.25 indicates upper edge of voxel at center and lower edge of the voxel at the edge of curve; red curve: Z –0.25 indicates lower edge of voxel at center and upper edge of the voxel at the edge of the curve).

#241860 Received 27 May 2015; revised 28 Jul 2015; accepted 30 Jul 2015; published 5 Aug 2015

4. Discussion

This study compared retinal shape between MRI and PCI modeling estimates and between MRI and Dunne's method. A set of procedures were required to obtain retinal shapes in terms of non-rotationally symmetric conicoids from MRI images. This included fits using 35% of the retinal area in order to be comparable with the region covered by PCI and peripheral refraction measurements. Modeling to obtain retinal shape from PCI was done in three levels of sophistication, all using variants of the Le Grand model eye.

In several cases there were significantly different estimates for both r_v and Q between the methods, but it was clear often that there was compensation such as a positive change in Q, in one method, relative to the other, compensating for a positive change in r_v. Therefore, as a better approach, "surface shapes" were compared between the methods. The results showed good agreement (within the theoretical uncertainty of MRI of 12-14%) between MRI and all three stages of PCI modeling (4% along horizontal meridian and 6% error along the vertical meridian), but not as good between MRI and Dunne's method (6% along the horizontal meridian and 9% along the vertical meridian). Thus, all the PCI stages would appear to give better estimates of retinal shape than Dunne's method. It is possible that the Dunne's method would provide better agreement with MRI results with a different basic model, but this was not pursued.

The percentage differences between MRI and PCI or between Dunne's method and MRI were not affected significantly by refraction group (emmetropes versus myopes), with p-values for independent t-tests being ≥ 0.28 for PCI and 0.08 and 0.43 for Dunne's method.

For the majority of participants, all three stages of the PCI modeling and the Dunne's method gave flatter estimates of retinal shape than did MRI, with the differences being smaller along the horizontal than along the vertical meridian. This variation between the MRI and other methods could be due in part to the large voxel size of the MRI images (0.5 mm) which influences the edge detection routine used in determining retinal shape estimates as it determines the transition between voxels that are purely vitreous to those that are solely in the sclera. Another possible reason for discrepancies between the MRI and other methods could be the different percentages of retinal area of 35% for MRI and 27% for horizontal (± 35°) and 23% vertical meridians (± 30°) for both PCI and Dunne's method. It is possible that our Stage 3 estimates may have been closer to MRI if we had included accurate data for the posterior corneal surface and had access to more information about lens structure including gradient index variation.

The reason for better agreement between MRI and the other two methods for the horizontal meridian than for the vertical meridian might be related to the PCI and Dunne's methods sampling 15 points out to ± 35° in the horizontal meridian and 13 points out to ± 30° in the vertical meridian.

It is likely that the three stages of the PCI modeling give similar results because the assumption that infrared beams are directed normal to the anterior cornea is reasonable and that beams are directed close to the nodal points of the eye so that the deviation within the eye is small. In Atchison and Charman's [18] theoretical work using variations on the Gullstrand number 1 eye, they found that Stage 1 was highly accurate out to at least ± 40°.

Another possible instrumentation that can be used for determining retinal shape is optical coherence tomography, which is based on PCI. Although there are issues with optical distortion of the retinal images, this can be corrected potentially by using optically based algorithms [30–32]. Kuo et al. [30] estimated retinal shapes in terms of retinal radius of curvature using OCT, whereas the current study determined retinal shapes in terms of conicoids. Differences between the instrumentation for determining retinal shape need further investigation.

From this study, for the PCI modeling the Stage 1 analysis was a very simple method assuming the parameters of the Le Grand model eye and ignoring light deviation within the

#241860 Received 27 May 2015; revised 28 Jul 2015; accepted 30 Jul 2015; published 5 Aug 2015

eye. The latter might lead to inaccurate results in the presence of irregular corneas or refractive myopia (either curvature or refractive index based). All stages of PCI modeling gave similar shape results as MRI, but Stage 2 and Stage 3 gave slightly different retinal co-ordinates than the simple Stage 1. Given the similar results for Stage 2 and 3, we recommended the use of Stage 2 rather than the sophisticated Stage 3. The methods developed here can be used in future studies for investigating the role for retinal shape in myopiogenesis.

Acknowledgments

This work was financially supported by Johnson & Johnson Vision Care, Inc., Florida. Authors thank the Centre for Advanced Imaging, University of Queensland, and in particular its radiographers Aiman Al Najjar and Anita Burns.

#241860 Received 27 May 2015; revised 28 Jul 2015; accepted 30 Jul 2015; published 5 Aug 2015